Human Exposure to Wireless Power Transmitter over Real Ground

Petra Rašić, Zoran Blažević, Dragan Poljak, and Maja Škiljo

Original scientific article

Abstract—The paper undertakes a comparative examination between a novel analytical methodology and a conventional numerical technique to analyze human exposure to electromagnetic fields emitted by a vertically positioned, electrically short antenna over a real homogeneous ground. In this investigation, the human body is represented as a vertically and horizontally positioned homogeneous cylinder, accounting for resonant and non-resonant frequencies, and corroborated with numerical simulations utilizing realistic human body models in FEKO software. The influence of the earth-air interface on real ground is considered by incorporating Fresnel's reflection coefficients. The analytical solution entails solving the Pocklington equation using the method of variation of constants, while the corresponding reflected field is determined through field integral evaluations. The innovative analytical approach adopts an approximate sinusoidal current distribution and analytical assessment of field integrals. The research demonstrates satisfactory alignment between these two methodologies and extends the previous analytical model by validating it with realistic human body models positioned over real ground, thereby increasing its complexity and practical applicability.

Index Terms—analytical approach, reflected near field, numerical solution procedures, human exposure, WPT, ICNIRP.

I. INTRODUCTION

Accurate modeling of human exposure to electromagnetic fields (EMFs) is critical, especially in wireless power transfer (WPT) systems, where the transfer of larger powers may occur. This requires precise tissue modeling and dielectric property definitions. However, no universally accepted methods exist for measuring exposure, complicating the process as technologies evolve. Researchers aim to develop reliable measurement methods that ensure human safety without overestimating risks, which could hinder system implementation [1]. Concerns about EMF exposure, particularly for frequencies $f < 400$ MHz range used by WPT systems, have led to updated safety guidelines in 2019 and 2020 [2], [3].

Mathematical modeling of human EMF exposure often involves solving differential, integral, or variational equations, and offers little or no possibility of connecting the exposure parameters to the system parameters directly, through relatively simple formulas as in analytical methods. However,

analytical modeling is feasible only for simple cases, while numerical approaches can address complex scenarios but may introduce inaccuracies [4]. Thus, the approach to analysis by combination of analytical and full-wave modeling could have real-life applications in ensuring human safety around WPT systems, such as wireless electric vehicle (EV) charging stations, medical device charging, and consumer electronics like smartphones and wearables. It could also be used in industrial automation, smart homes, and public transport systems to minimize exposure to EMF while optimizing power transfer efficiency.

Recent studies, such as [5], used Monte Carlo simulations to explore low-frequency EMF effects on 3D human models, while [6], [7] applied boundary element modeling to study the influence of low-frequency (LF) fields. Other research, including [8], [9], and [10], investigated extremely low-frequency (ELF) fields and maternal exposure effects on child development. Studies [11] and [12] also examine Specific Absorption Rate (SAR) compliance, finding exposure varies with body models and proximity to sources. [10] shows SAR remains within safety limits for 45 W power at 8 MHz, aligning with this paper's findings, while [12] explores Transmitted Power Density (TPD) for near-field exposures at lower frequencies.

This paper focuses on the challenges of near-field WPT exposure, using an analytical modeling approach based on antenna theory. It assesses human exposure to EMFs in a scenario involving a human subject and an antenna over lossy ground, transmitting at frequencies of 13.56 MHz and 86.33 MHz. The analysis includes neuromuscular simulations to evaluate the induced electric field, SAR, and TPD, comparing these values with international standards.

The analysis contributes to understanding human exposure to EMFs in WPT systems by introducing a novel analytical modeling approach based on Pocklington-type equations. This approach compares results from analytical and numerical models, highlighting discrepancies and agreements in predicting human exposure. Our previous studies [13], [14], and [15] focus on developing and validating the analytical model considering its limitations, where the analytical results were tested on straight cylinder by comparison with the results obtained by full-wave model, King's three-term approximate model [16], and the far-field approximation model [4]. This study enhances the model by validating a transmitter near a realistic human model positioned above the real ground, introducing greater complexity and practical significance, with a focus on contrasting its behavior with Perfect Electrical Conductor

(PEC) ground conditions.

Furthermore, the study evaluates WPT systems at industrial, scientific and medical (ISM) use frequency of 13.56 MHz, and at 86.33 MHz which is resonant frequency of the cylinder representing an average human, ensuring compliance with safety guidelines and addressing public health concerns. Using anatomically realistic human models, the paper enhances the accuracy of exposure assessments, which is crucial for reliable safety evaluations and system design. The numerical results of the simulations, validated against analytical predictions and experimental data using FEKO software, confirm the reliability of the proposed methods. The research also identifies future investigation areas, focusing on how different human models and distances from sources affect exposure outcomes.

The paper is structured as follows. Section II covers the analytical framework for assessing exposure in WPT systems, Section III details FEKO software simulations and validation, and Section IV summarizes key findings, addressing safety considerations and future research areas for high-frequency (HF) transmitting antennas in WPT systems.

II. ANALYTICAL FORMULATION

Consider a mixed TE_{10}/TM_{10} ideal point source (transmitter T_x) above real ground at a height h illuminating a straight thin cylinder of the length L and the radius a not electrically connected to the soil, as depicted in Figure 1. In this sense, two cases are considered: a thin vertical cylinder that is not electrically connected to the ground, and a horizontal cylinder at a height H above the ground. The parameters of the ground and the cylinder include their permittivity ε_r and conductivity σ. The complex permittivity can be represented by the following expression:

$$\varepsilon_c = \varepsilon_r - j60\sigma\lambda \tag{1}$$

A. Incident Electric Field

The illustration in Figure 1 portrays the situation of a vertically-oriented electrically small dipole generating TE_{10}/TM_{10} modes at a height h above an infinite ground plane. The radiated electric field $\vec{E} = E_r \vec{e_r} + E_\theta \vec{e_\theta} + E_\phi \vec{e_\phi}$, which is a function of the frequency f and the distance r [17], [18], is calculated as:

$$\vec{E}(\vec{r}, f) = \beta \sqrt{\frac{3PZ_0}{4\pi(1+\alpha^2)}} \left\{ e_r^2 \left[\frac{1}{(j\beta r)^2} + \frac{1}{(j\beta r)^3} \right] \cos\theta \right.$$
$$+ \vec{e_\theta} \left[\frac{1}{j\beta r} + \frac{1}{(j\beta r)^2} + \frac{1}{(j\beta r)^3} \right] \sin\theta$$
$$\left. + \vec{e_\phi} j\alpha \left[\frac{1}{j\beta r} + \frac{1}{(j\beta r)^2} \right] \sin\theta \right\} e^{-j\beta r}$$
$$\tag{2}$$

where $Z_0 = 120\pi$ Ω is the free-space impedance, $\beta = 2\pi/\lambda = 2\pi f/c$, c being the velocity of light and λ is the wavelength.

The mode ratio is $\alpha = \sqrt{\frac{P_{TE}}{P_{TM}}}$, P_{TE} and P_{TM} represent the radiated powers of TE mode and TM mode, respectively, whereas $P = P_{TE} + P_{TM}$ is the total radiated power.
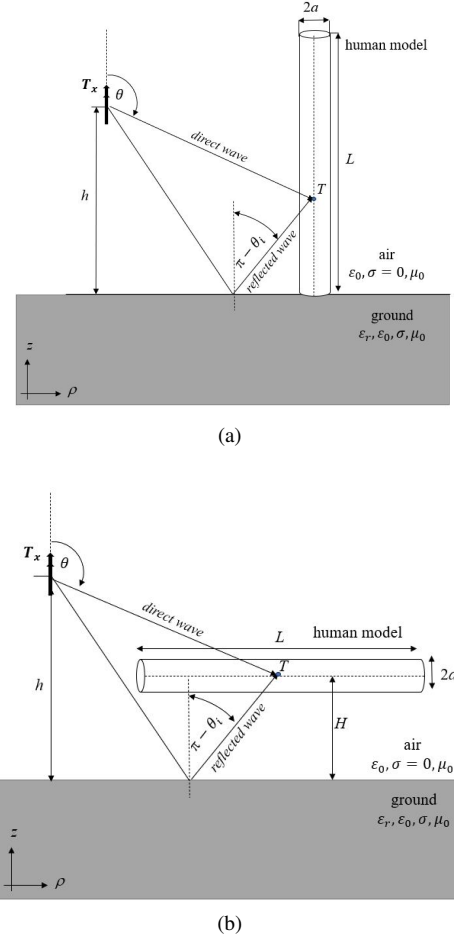

(a)

(b)

Fig. 1. Ideal electric/magnetic point source illuminating a cylinder above a real ground (2D view in the plane of incidence) in case of (a) vertically, (b) horizontally positioned cylinder.

The observed field at point T in space results from the combination of two components:

$$\vec{E}(T) = \overrightarrow{E_{\text{dir}}}(T) + \overrightarrow{E_{\text{ref}}}(T) \tag{3}$$

where $\overrightarrow{E_{dir}}(T) = \vec{E}(\vec{r_0})$ the direct wave component constitutes one aspect, while the component reflected from the ground can be readily determined in cylindrical coordinates using Modified Image Theory (MIT) as:

$$\overrightarrow{E_{\text{ref}}}(T) = R_H \left[\vec{E}(\vec{r_i})\vec{e_\phi} \right] \vec{e_\phi} + R_V \left\{ \left[\vec{E}(\vec{r_i})\vec{e_z} \right] \vec{e_z} \right.$$
$$\left. - \left[\vec{E}(\vec{r_i})\vec{e_\rho} \right] \vec{e_\rho} \right\} \tag{4}$$

where r_i refers to the distance from the image of a source to a point T of interest.

In spherical coordinates:

$$\overrightarrow{E_{\text{ref}}} = R_H E_\phi \vec{e_\phi} + R_V (E_r \cos 2\theta_i - E_\theta \sin 2\theta_i) \vec{e_r}$$
$$- R_V (E_r \sin 2\theta_i + E_\theta \cos 2\theta_i) \vec{e_\theta} \tag{5}$$

The reflection coefficients R_H and R_V are designated based on whether the signal is horizontally or vertically polarized,

respectively. Given that the angle of the reflected ray in relation to the ground plane is $\theta_i - \pi/2$ (refer to Fig. 1), their Fresnel plane-wave approximation can be formulated as:

$$R_V = \frac{\left(\varepsilon_c \cos\theta_i + \sqrt{\varepsilon_c - \sin^2\theta_i}\right)}{\left(\cos\theta_i - \sqrt{\varepsilon_c - \sin^2\theta_i}\right)} \tag{6}$$

$$R_H = \frac{\left(\cos\theta_i + \sqrt{\varepsilon_c - \sin^2\theta_i}\right)}{\left(\cos\theta_i - \sqrt{\varepsilon_c - \sin^2\theta_i}\right)} \tag{7}$$

B. Current along the Cylinder

Once the incident electric field is known, the current induced along the straight thin cylinder can be calculated. It is governed by the Pocklington integral-differential equation [4]:

$$\int_0^L \left(\frac{\partial^2}{\partial l^2} + \beta^2\right) I(l') g(l,l') \, \mathrm{d}l' - j4\pi\frac{\beta}{z_0} Z_S(l)I(l) = \\ -j4\pi\frac{\beta}{z_0} E_z(l) \tag{8}$$

Here, $E_z(l)$ represents the excitation in the form of tangential electric field, Z_0 denotes the free space impedance, $I(l')$ signifies the current distribution on the wire, and $g(l,l')$ refers to the Green function.

The surface impedance is expressed in [19] as:

$$Z_S(\zeta) = \frac{Z}{2\pi a} \frac{J_0(\gamma_w, \zeta)}{J_1(\gamma_w, a)} \tag{9}$$

In this expression, J_0 and J_1 denote the zeroth and first-order Bessel functions, respectively, and $0 \leq \zeta \leq a$. The quantities Z and γ_w are defined as:

$$Z = \sqrt{\frac{j\omega\mu}{\sigma + j\omega\varepsilon}} \tag{10}$$

$$\gamma_w = \sqrt{j\omega\mu(\sigma + j\omega\varepsilon)} \tag{11}$$

Here, $\varepsilon = \varepsilon_r\varepsilon_0$ represents the permittivity, where ε_r is the relative permittivity and ε_0 is the vacuum permittivity. Assuming that the current varies slowly, i.e., $I(I) \approx I(l')$, and vanishes at the end of the cylinder, the Pocklington equation transforms into a simpler form of a differential equation [4]:

$$\left[\frac{\partial^2}{\partial l^2} + \gamma^2(l)\right] I(l) = -j4\pi\frac{\beta}{\psi(l)z_0} E_z(l) = F(l) \tag{12}$$

where

$$\psi(l) = \int_0^L g(l,l') \, \mathrm{d}l' \tag{13}$$

and:

$$\gamma^2 = \beta^2 - j4\pi\frac{\beta}{\psi(l)Z_0} Z_S(l) \tag{14}$$

Analytically seeking the general solution of (12) is not feasible due to γ being a function of the position l along

the cylinder. The Green function for the perpendicular wire positioned above the lossy ground is provided in [4]:

$$g(l,l') = g_0(l,l') + R_V|_{\angle_i=\frac{\pi}{2}} g_i(l,l') \tag{15}$$

and for the horizontal cylinder above ground:

$$g(l,l') = g_0(l,l') - R_V|_{\angle_i=\frac{\pi}{2}} g_i(l,l') \tag{16}$$

where $g_0(l,l')$ is the free space Green function:

$$g_0(l,l') = \frac{e^{-jkr}}{r} \tag{17}$$

and $g_i(l,l')$ originates from the principles of image theory:

$$g_i(l,l') = \frac{e^{-jkr_i}}{r_i} \tag{18}$$

The parameters r_0 and r_i represent the distances from the source and image antenna to the observation point, respectively. As stated in [4], (13) can be simplified when considering a straight thin wire perpendicular to the ground:

$$\psi(l) = 2\left(\ln\frac{L}{a} + R_V|_{\angle_i=\frac{\pi}{2}} \ln 2\right) \tag{19}$$

or parallel to ground:

$$\psi(l) = 2\left(\ln\frac{L}{a} - R_V|_{\angle_i=\frac{\pi}{2}} \ln\frac{L}{2H}\right) \tag{20}$$

where $R_V|\angle_i = \frac{\pi}{2}$ is the reflection coefficient calculated by (6) for an angle of incidence of $90°$ ($\theta_i = \pi$) as in [4]. Using Fresnel reflection coefficients instead of Sommerfeld integrals can simplify calculations, although this might come at the cost of reduced accuracy. This approach is practical when exact precision is not crucial, or when rapid, real-time computations are needed. While Sommerfeld integrals offer higher accuracy in complex environments, such as multilayer media, they are computationally demanding. The Fresnel reflection coefficients provide a reasonable compromise when prioritizing speed and simplicity, but for scenarios requiring high precision in complex conditions, Sommerfeld integrals are more appropriate.

Utilizing the boundary conditions for the ends of the cylinder, namely $I(0) = I(L) = 0$, the general solution for the current flowing through the cylinder axis is provided as [4]:

$$I(l) = I_0(l) - \frac{I_0(0)\sin[\gamma(L-l)] + I_0(L)\sin(\gamma l)}{\sin(\gamma L)} \tag{21}$$

Here, $I_0(l)$ represents the particular solution of (12), expressed as the infinite sum of even derivatives of the excitation function:

$$I_0(l) = \frac{1}{\gamma^2} \sum_{n=0}^{\infty} \frac{F^{(2n)}(l)}{(j\gamma)^{2n}} \tag{22}$$

Here, $F^{(0)}(l)$ denotes $F(l)$. In its most basic form, if the incident electric field on the cylinder changes slowly, it is feasible to disregard all terms in (21) except the first one, yielding $I_0(l) \approx F(l)/\gamma^2$. This offers an approximation of the

current that still satisfies the boundary conditions, expressed as:

$$I(l) \approx \frac{1}{\gamma^2} \left\{ F(l) - \frac{F(0)\sin[\gamma(L-l)] + F(L)\sin(\gamma l)}{\sin(\gamma L)} \right\} \tag{23}$$

Here, $F(l)$ is obtained from (12) and is contingent upon the distribution of the incident electric field along the cylinder. The derived relationship represents a broader application of the current formula compared to the scenario of plane wave incidence detailed in [13].

C. Dosimetric Quantities

Once the axial current is determined, it becomes feasible to compute the current density within the body. In [4], the current density is formulated as:

$$\mathrm{J}(\zeta, l) = \frac{I(l)}{a^2\pi} \left(\frac{\beta a}{2} \right) \frac{J_0\left(j^{-1/2}\beta\zeta\right)}{J_1\left(j^{-1/2}\beta a\right)} \tag{24}$$

Here, ζ ranges from 0 to a, and J_0 and J_1 represent the respective Bessel functions. The induced electric field within the body is computed employing the method described in [4]:

$$E_{in}(\zeta, l) = \frac{\mathrm{J}(\zeta, l)}{\sigma + j\omega\varepsilon} \tag{25}$$

Here, ρ denotes the tissue density, while σ and ε pertain to the electrical properties of the human body.

Consequently, the SAR is determined as:

$$SAR = \sigma \frac{|E_{in}(\zeta, l)|^2}{\rho} \tag{26}$$

The SAR averaged over every 10 grams of tissue (SAR_{10g}, when considering a model like a cube, it means that the average absorbed energy is calculated in a 10-gram volume V_{10g} of the cube with side length a_c), expressed in Cartesian coordinates, is provided by the expression given in [4]:

$$\begin{aligned} SAR_{10g} &= \frac{1}{V_{10g}} \iiint SAR \, dV_c \\ &= \frac{1}{V_{10g}} \int_0^{a_c} \int_0^{a_c} \int_0^{a_c} SAR \, dx_c \, dy_c \, dz_c \end{aligned} \tag{27}$$

The whole-body average SAR (SAR_{WB}) expressed in cylindrical coordinates is determined by the expression also provided in [4]:

$$\begin{aligned} SAR_{WB} &= \frac{1}{V} \iiint SAR \, dV \\ &= \frac{1}{V} \int_0^a \int_0^{2\pi} \int_0^L SAR \, \zeta \, d\zeta \, d\varphi \, dl \end{aligned} \tag{28}$$

Here, V represents the volume of the cylinder, and the surface SAR is defined as in (26). By employing Equations (24) to (27) and making certain mathematical adjustments, Equation (28) is expressed in integral form as:

$$\begin{aligned} SAR_{WB} =\ & \frac{1}{\sigma^3} \frac{1}{1 + (\omega\tau)^2} \left(\frac{\beta}{a^2\pi} \right)^2 \\ & \times \frac{\int_0^a \zeta \left| J_0\left(j^{-1/2}\beta\zeta\right) \right|^2 d\zeta}{2\rho L \left| J_1\left(j^{-1/2}\beta a\right) \right|^2} \int_0^L |I(l)|^2 dl \end{aligned} \tag{29}$$

Here, $\tau = \varepsilon/\sigma$ denotes the charge relaxation time. Additionally, the transmitted power density (TPD) is defined following [13] as:

$$TPD(l) = \frac{1}{2} \int_\zeta^a \sigma \left| E_{in}(\zeta, l) \right|^2 d\zeta \tag{30}$$

Here, σ represents tissue conductivity. TPD is a quantity that was primarily introduced for the GHz frequency range due to surface effects being more pronounced under these conditions. Although its primary use is in high-frequency applications, it can also be applied in lower frequency ranges. However, it is important to note that its relevance at lower frequencies may be limited, depending on the specifics of the application.

By taking into account Equations (24) to (25), Equation (30) can be formulated as:

$$\begin{aligned} TPD =\ & \frac{1}{8\sigma^3} \frac{1}{1 + (\omega\tau)^2} \left(\frac{\beta a}{a^2\pi} \right)^2 \\ & \times \left| \frac{I(l)}{J_1\left(j^{-1/2}\beta a\right)} \right|^2 \int_\zeta^a \left| J_0\left(j^{-1/2}\beta\zeta\right) \right|^2 d\zeta \end{aligned} \tag{31}$$

III. NUMERICAL RESULTS

The electromagnetic modeling of the resonant WPT transmitter above ground was conducted utilizing the commercial software FEKO, employing the Method of Moments (MoM) for wire antenna analysis. To ensure accurate representation of the dielectric body models with specific parameters, the Surface Equivalence Principle (SEP) was applied, following guidelines from the IT'IS database [19].

In the exposure scenario, an ideal short electric dipole perpendicular to ground radiating in TM_{10} mode was selected as the radiation source. A voltage source was applied to port 1 at frequencies of $f = 13.56$ MHz (ISM band), and of $f = 86.33$ MHz that is half-wave resonant with the cylinder. This frequency choice was made considering also the characteristics of the lossy ground, with relative permittivity $\varepsilon_r = 4$ and conductivity $\sigma = 1 \times 10^{-3}$ mS/m [19], indicating that the ground exhibits more insulator-like properties at the considered frequencies.

In accordance with the WPT standard [20], the matched transmitting antenna input power was set to $P_G = 5$ W. This parameter serves as a reference point for assessing the efficiency and performance of the WPT system. By employing these specific parameters and methodologies, the electromagnetic modeling aims to accurately characterize the behavior of the WPT system, evaluate potential exposure levels, and ensure compliance with safety standards and regulations.

In the electromagnetic modeling setup, the human body is represented as a cylinder with specific geometric dimensions.

The cylinder is 1.8 m long and has diameter of 0.18 m, providing a simplified yet representative approximation of the human body shape. Additionally, the wire antenna used in the model has a radius of 8 mm, while the length of the edge of the triangle in the human body model representation measures 35 mm. These dimensions are chosen to ensure accuracy in simulating electromagnetic interactions with the human body.

In FEKO, a human model without arms is used to avoid current spikes in areas with thin cross-sections. Thin regions, such as arms, can cause undesired current jumps due to the large difference in cross-sectional dimensions, complicating accurate simulations. Modeling a human without arms, which is geometrically more similar to a cylinder, allows for easier and more accurate calculations as cylindrical geometry is simpler for numerical processing and better matches the distribution of electromagnetic fields without unexpected singularities.

In Figs. 2 and 3, the ideal short electric dipole radiating in TM_{10} mode is positioned in front of the cylinder at a height of 1.2 m. This configuration corresponds to the worst-case scenario described in [21], allowing for a comprehensive assessment of exposure levels and potential risks. The distances from the center of the human body model to the center of the dipole are denoted by the values $d_{p1} = 35$ cm and $d_{p2} = 65$ cm, providing insight into the spatial distribution of electromagnetic fields and their impact on human exposure.
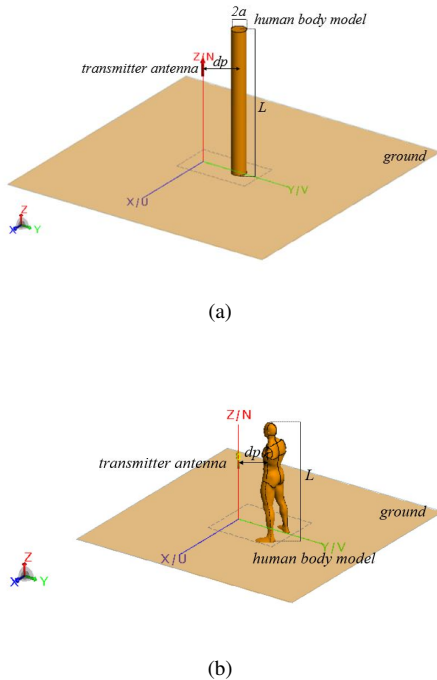

(a)

(b)

Fig. 2. (a) Simplified equivalent vertically positioned cylinder standing against the transmitting short dipole, and (b) realistic human body model human body model.

The results obtained from the electromagnetic simulations and calculations are presented in Figs. 4 to 11, offering a detailed visualization of key parameters such as induced electric field, SAR_{10g}, SAR_{WB}, and TPD using relations 26, 28, 30 and 32, respectively. These figures provide valuable insights into the distribution and intensity of electromagnetic fields around the human body in proximity to the radiating antenna.

By analyzing these results, researchers can gain a deeper understanding of potential exposure risks and devise appropriate safety measures to mitigate any adverse effects. Overall, the combination of geometric modeling, antenna placement, and numerical simulations enables a comprehensive evaluation of human exposure to electromagnetic fields in WPT systems. These findings contribute to the ongoing efforts to ensure the safety and reliability of WPT technologies for various applications.
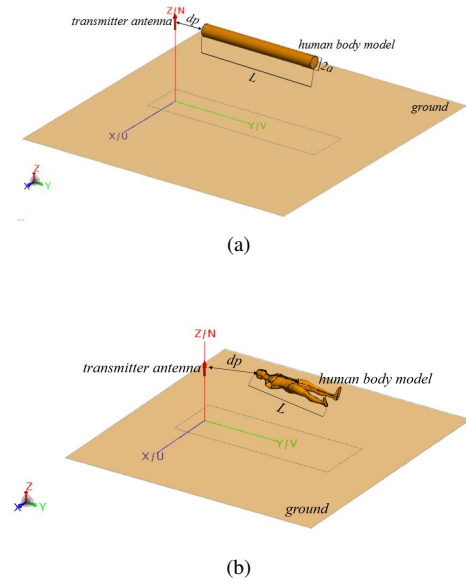

(a)

(b)

Fig. 3. (a) Simplified equivalent horizontally positioned cylinder standing against the transmitting short dipole, and (b) realistic human body model human body model.

The analysis of the numerical data presented in the figures indicates that the analytical results generally align well with the numerical results across various scenarios. However, certain differences are more noticeable, especially at locations where there are maximum peaks in the data.

When considering the simulations involving realistic numerical human body models, the numerical results tend to yield higher amplitude values compared to both the simplified numerical model and the proposed analytical model. The analytical model falls in between these two extremes.

One key observation is that, besides that the trend and distribution of the results are in good agreement, when the transmission occurs at the non-resonant ISM frequency of the cylinder the maximum exposure can be expected at positions closest to the Tx antenna, whereas at the resonant frequency it is expected in the middle of the body.
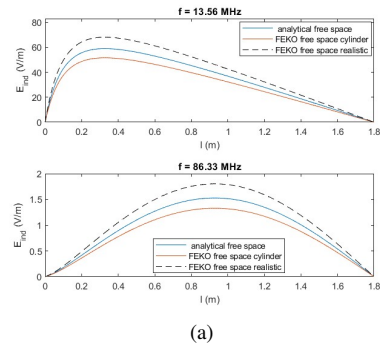
As anticipated, the TPD (Figs. 8 to 11) exhibits peak values at the closest distance to the transmitter antenna, which is a common observation in electromagnetic field exposure scenarios [4].
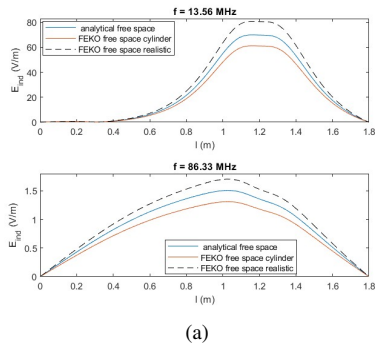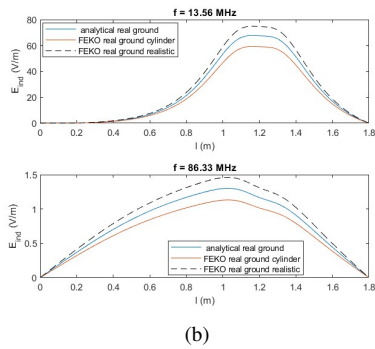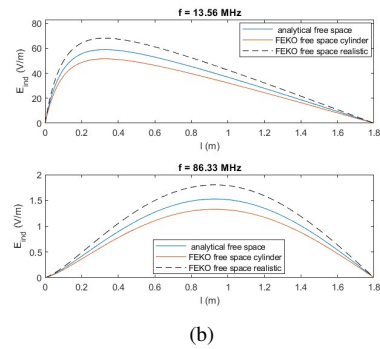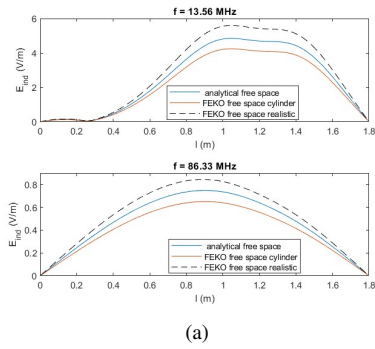
Fig. 4. Induced electric field along the vertically positioned human body model for $d_{p1} = 35$ cm in case of (a) free space, (b) real ground.
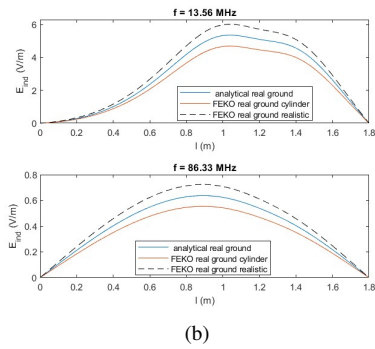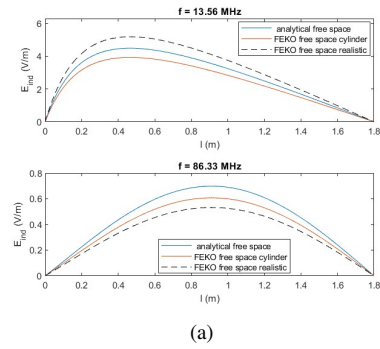

Fig. 6. Induced electric field along the horizontally positioned human body model for $d_{p1} = 35$ cm in case of (a) free space, (b) real ground.
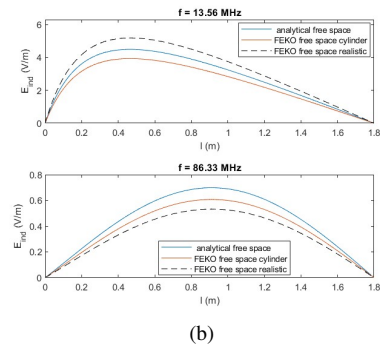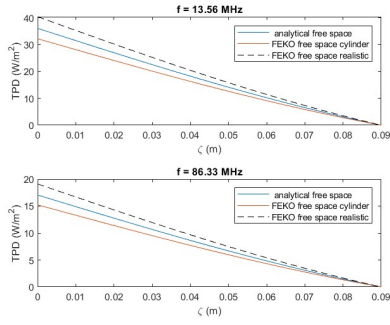

Fig. 5. Induced electric field along the vertically positioned human body model for $d_{p1} = 65$ cm in case of (a) free space, (b) real ground.
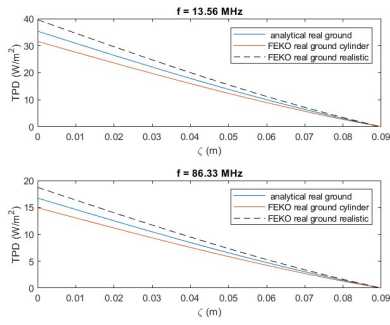

Fig. 7. Induced electric field along the horizontally positioned human body model for $d_{p2} = 65$ cm in case of (a) free space, (b) real ground.

Fig. 8. TPD along the vertically positioned human body model for $d_{p1} = 35$ cm in case of (a) free space, (b) real ground.

Fig. 9. TPD along the vertically positioned human body model for $d_{p2} = 65$ cm in case of (a) free space, (b) real ground.

Fig. 10. TPD along the horizontally positioned human body model for $d_{p1} = 35$ cm in case of (a) free space, (b) real ground.

Fig. 11. TPD along the horizontally positioned human body model for $d_{p2} = 65$ cm in case of (a) free space, (b) real ground.

TABLE I
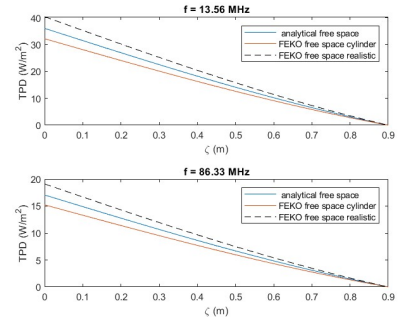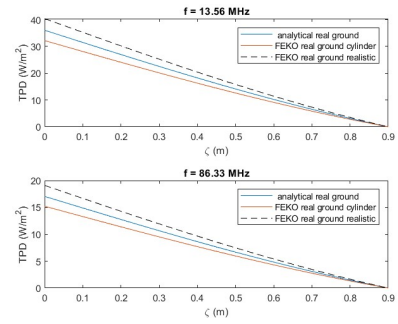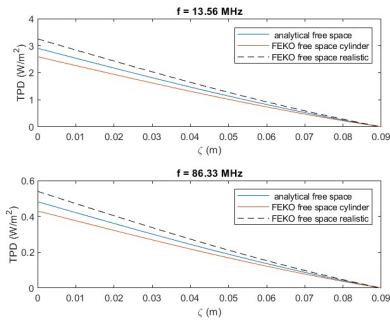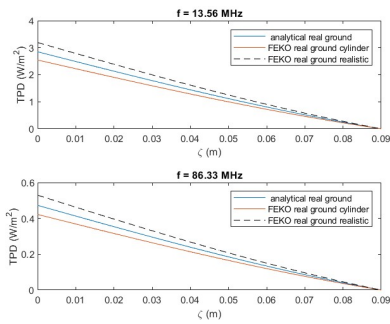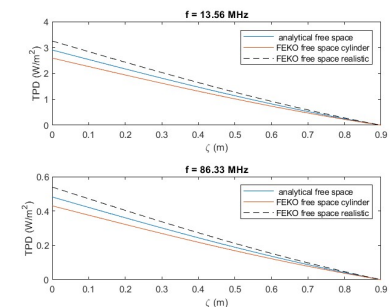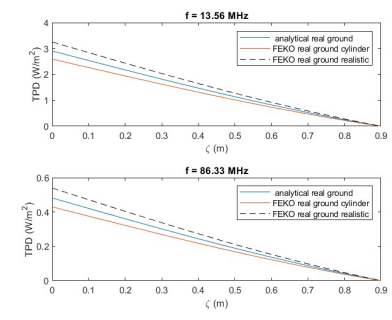COMPARISON AMONG MAXIMUM VALUES OF SAR_{10g} AND THE
FUNDAMENTALS OF ICNIRP [2].

SAR$_{10g}$ (W/kg)					ICNIRP SAR$_{10g}$ limits (W/kg)	
f = 13.56 MHz	ground		free space		General public	Workers
	d_{p1}	d_{p2}	d_{p1}	d_{p2}		
proposed analytical	1.74424	0.26189	1.83142	0.27498		
FEKO cylinder	1.53489	0.23423	1.61163	0.24594		
FEKO realistic	1.93384	0.29545	2.03053	0.31022		
					2	10
f = 86.33 MHz	d_{p1}	d_{p2}	d_{p1}	d_{p2}		
proposed analytical	0.26995	0.11112	0.28339	0.11665		
FEKO cylinder	0.24537	0.09991	0.25756	0.10489		
FEKO realistic	0.30124	025473	0.3162	0.26743		

TABLE II
COMPARISON AMONG MAXIMUM VALUES OF SAR_{10g} AND THE
FUNDAMENTALS OF ICNIRP [2].

SAR$_{10g}$ (W/kg)					ICNIRP SAR$_{10g}$ limits (W/kg)	
f = 13.56 MHz	ground		free space		General public	Workers
	d_{p1}	d_{p2}	d_{p1}	d_{p2}		
proposed analytical	1.42697	0.25930	1.81329	0.272265		
FEKO cylinder	1.51969	0.23191	1.59567	0.24350		
FEKO realistic	1.91469	0.29252	2.01043	0.30715		
					2	10
f = 86.33 MHz	d_{p1}	d_{p2}	d_{p1}	d_{p2}		
proposed analytical	0.2673	0.1100	0.2806	0.1155		
FEKO cylinder	0.2429	0.0989	0.2550	0.1039		
FEKO realistic	0.2983	0.2522	0.3131	0.2648		

TABLE III
COMPARISON AMONG MAXIMUM VALUES OF SAR_{WB} AND THE
FUNDAMENTALS OF ICNIRP [2].

SAR$_{WB}$ (W/kg)					ICNIRP SAR$_{WB}$ limits (W/kg)	
f = 13.56 MHz	ground		free space		General public	Workers
	d_{p1}	d_{p2}	d_{p1}	d_{p2}		
proposed analytical	0.01716	0.00257	0.01795	0.00262		
FEKO cylinder	0.01518	0.00244	0.01585	0.00231		
FEKO realistic	0.01893	0.00289	0.01984	0.00294		
					0.08	0.4
f = 86.33 MHz	d_{p1}	d_{p2}	d_{p1}	d_{p2}		
proposed analytical	0.00262	0.00107	0.00275	0.00112		
FEKO cylinder	0.00238	0.00097	0.00249	0.00100		
FEKO realistic	0.00292	0.00247	0.00306	0.00259		

TABLE IV
COMPARISON AMONG MAXIMUM VALUES OF SAR_{WB} AND THE
FUNDAMENTALS OF ICNIRP [2].

SAR$_{WB}$ (W/kg)					ICNIRP SAR$_{WB}$ limits (W/kg)	
f = 13.56 MHz	ground		free space		General public	Workers
	d_{p1}	d_{p2}	d_{p1}	d_{p2}		
proposed analytical	0.01700	0.0025	0.0178	0.0026		
FEKO cylinder	0.01503	0.0022	0.0157	0.0026		
FEKO realistic	0.01874	0.0029	0.0196	0.0029		
					0.08	0.4
f = 86.33 MHz	d_{p1}	d_{p2}	d_{p1}	d_{p2}		
proposed analytical	0.0026	0.0011	0.0027	0.0011		
FEKO cylinder	0.0024	0.0010	0.0025	0.0010		
FEKO realistic	0.0029	0.0024	0.0030	0.0026		

The comparison among the exposure results in Figs. 4 and 5 shows that there is no significant effect produced by introducing the real ground in the scenario (provided that the radiated power is equal in both, the free-space and the half-space scenario).

This is in consistence with the results of the PEC ground scenario depicted in [13]. Therefore, it can be concluded that,

for the fast initial assessments of the human exposure, the free-space scenario is quite sufficient.

This conclusion is further confirmed by observing the results in Figs. 6 and 7 for the horizontal cylinder above a real half-space. Also, although the induced field distribution at 13.56 MHz (ISM) is different from the case of the vertical cylinder as expected, it shows consistency when the cylinder is in resonance. There is a significant difference between the non-resonant ISM frequency and the resonant frequency scenario. In the first case, the maximum exposure is determined by the relative position of the source and the cylinder, whereas in the second case it is always in the middle regardless of the source position.

It is important to note that, although at the resonant frequency we expect significantly lower field values compared to the operating frequency, it is difficult to directly compare these values. However, we observe that, while at the operating frequency the dosimetric effect is mostly concentrated in the area nearest to the transmitting antenna, at the resonant frequency it is much more evenly distributed with the maximum at the middle of the cylindrical body.

In the context of the analyzed parameters, the proposed analytical approach tends to overestimate values in comparison with cylinder human body model. This overestimation is acceptable in terms of human impact, as higher values allow for more conservative safety measures, for example SAR which is shown in Tables I-IV. The Tables represent specific exposure parameters (SAR) obtained by simulations and compared with applicable safety limits (basic ICNIRP guidelines). These parameters are critical for ensuring compliance with ICNIRP guidelines, for workers and professionals [2].

However, in the case of the realistic human body model in FEKO, underestimation occurs, which is critical. For example, as the specific absorption rate (SAR) involves thermal effects, underestimating values can lead to incorrect exposure assessments. Note that in two specific cases (highlighted yellow in tables I, and II) the realistic model of human exhibits the exposure slightly above the limit, whereas the (both) cylinder models do not predict overexposure. Therefore, special attention must be put to the parameters that show underestimation to avoid safety oversights and ensure an accurate evaluation of human impact.

Furthermore, from the comparison of the results for the vertically (Figs. 4, 5) and the horizontally positioned (Figs. 6, 7) cylinder, it can be noted that the exposure is comparable between the two. Therefore, it can be concluded that the more complex scenarios such as a human sitting in a chair or like that, although could be modeled analytically by introducing proper boundary conditions, would lead only to a significantly more complex model but without significant new insights into the exposure issue.

The proposed analytical approach is compared with common numerical methods, including the MoM, FEM, and FDTD. In terms of accuracy, the proposed method shows a deviation of less than 10 % from the FEM results in calculating SAR and TPD, no matter cylinder or realistic human body model. This demonstrates its reliability for WPT applications. However, FDTD, relative to FEM and MoM methods, excels

in time-dependent scenarios and provides higher accuracy for complex human body models in non-homogeneous environments [4].

While FEM and MoM are effective for specific problem sets (e.g., boundary-specific conditions and steady-state solutions), the proposed method is more convenient in sense of time consuming for near-field modeling and scenarios involving low-power WPT systems at high frequency bands, such as 13.56 MHz and 86.33 MHz. However, for highly detailed body models with complex tissue structures, FDTD remains the preferred method for ensuring precise dosimetric calculations.

IV. CONCLUSION

The comparative analysis between numerical and proposed analytical methods shows consistent findings, validating both approaches in characterizing the antenna system. The study demonstrates the analytical framework's effectiveness in capturing essential electromagnetic field features, including induced electric field, SAR, and TPD, while numerical simulations offer a detailed understanding of complex dosimetry interactions.

By corroborating numerical and analytical results, the study enhances our understanding of the dosimetry phenomena over a lossy medium. It highlights the complementary nature of these methods, showcasing their collective ability to provide comprehensive insights into electromagnetic phenomena.

For example, while lower field values are expected at the resonant frequency compared to the ones at lower operating frequency, direct comparison is challenging. Nevertheless, the dosimetric effect at the resonant frequency is more evenly distributed throughout the cylinder, whereas it is concentrated in the area nearest to the transmitting antenna at the operating frequency departed from the resonance.

Overall, the combined use of numerical and analytical methods provides a robust approach to studying antenna systems, facilitating deeper insights into dosimetry characteristics and aiding in the design and optimization process.

REFERENCES

[1] World Health Organization, "from internet," https://www.who.int/pehemf/about/WhatisEMF/en/, [Jan 2023].
[2] ICNIRP, "Guidelines for limiting exposure to electromagnetic fields (100 khz to 300 ghz)," 2020.
[3] IEEE PC95.1/D3.5, "Ieee draft standard for safety levels with respect to human exposure to electric, magnetic and electromagnetic fields, 0 hz to 300 ghz," 2018, 1-312, October 2018.
[4] D. Poljak and M. Cvetkovic, *Human Interaction with Electromagnetic Fields*. Academic Press, 2019.
[5] e. a. C. Luz, "Monte carlo simulation of current densities in a 3d human body model exposed to low-frequency electromagnetic fields," *Frontiers in Public Health*, vol. 10, p. 795414, 2022.
[6] A. Peratta, D. Poljak, and M. Cvetković, "Boundary element modelling of human exposure to extremely low frequency electric fields: Computational aspects and applications," *Electronics*, vol. 11, no. 8, p. 1228, 2022.
[7] C. Gonzalez, A. Peratta, and D. Poljak, "Modelling the human body exposure to elf electric fields," in *Modelling in Medicine and Biology IX*, C. A. Brebbia, Ed. Southampton: WIT Press, 2010, pp. 245–254.
[8] A. Peratta, D. Poljak, and M. Cvetković, "Human body exposure to fixed potentials surfaces in power substations," *WIT Transactions on Biomedicine and Health*, vol. 12, pp. 1–6, 2022.
[9] D. Cavka, D. Poljak, A. Peratta, and C. A. Brebbia, "Boundary element modeling of human exposure to electrostatic fields generated by video display units," in *Boundary Elements and Other Mesh Reduction Methods XXX*, L. Škerget and C. A. Brebbia, Eds. Southampton: WIT Press, 2008, pp. 115–124.
[10] A. Bortkiewicz and E. Gadzicka, "Maternal exposure to extremely low frequency electromagnetic fields during pregnancy and its effects on child development," in *Proceedings of the 2020 International Conference on Environmental Health and Human Health*, 2020, pp. 45–52.
[11] A. Christ, M. G. Douglas, J. M. Roman, E. B. Cooper, A. P. Sample, B. H. Waters, J. R. Smith, and N. Kuster, "Evaluation of wireless resonant power transfer systems with human electromagnetic exposure limits," *IEEE Trans. Electromagn. Compat.*, vol. 55, no. 2, pp. 265–274, 2013.
[12] X. L. Chen, A. E. Umenei, D. W. Baarman, N. Chavannes, V. De Santis, J. R. Mosig, and N. Kuster, "Human exposure to close-range resonant wireless power transfer systems as a function of design parameters," *IEEE Trans. Electromagn. Compat.*, vol. 56, no. 5, pp. 1027–1034, 2014.
[13] P. Rašić, Z. Blažević, D. Poljak, and M. Škiljo, "Analytical versus numerical approach to the analysis of the wireless power transmitter human exposure over real ground," in *2024 9th International Conference on Smart and Sustainable Technologies (SpliTech)*, 2024, pp. 1–6.
[14] P. Rašić, Z. Blažević, and D. Poljak, "Assessment of human exposure to high frequency fields generated by wireless transmitters: A simplified analytical model," *PIER B Progress in Electromagnetics Research B*, 2023.
[15] P. Rašić, Z. Blažević, D. Poljak, and M. Škiljo, "A simplified analytical model for human exposure to electromagnetic radiation of hf wireless power transmitter," in *2022 7th International Conference on Smart and Sustainable Technologies (SpliTech)*, 2022, pp. 1–6.
[16] S. J. Orfanidis, "Electromagnetic waves and antennas," https://eceweb1.rutgers.edu/~orfanidi/ewa/ewa-1up.pdf, [Nov 2024].
[17] J. Lee and S. Nam, "Fundamental aspects of near-field coupling small antennas for wireless power transfer," *IEEE Trans. Antennas Propag.*, vol. 58, no. 12, pp. 3442–3449, 2010.
[18] C. A. Balanis, *Antenna Theory: Analysis and Design*, 4th ed. John Wiley and Sons, Inc., 2016.
[19] IT'IS, "database, from internet," http://www.itis.ethz.ch/virtual-population/tissue-properties/database/dielectric-properties, [Jan 2023].
[20] ITU, "database, from internet," https://itu.int/dms_pubrec/itu-r/rec/p/R-REC-P.527-4-201706-I!!PDF-E.pdf, [Jan 2023].
[21] R. Tseng, B. von Novak, S. Shevde, and K. A. Grajski, "Introduction to the alliance for wireless power loosely-coupled wireless power transfer system specification version 1.0," in *Proceedings of Wireless Power Transfer (WPT)*, Perugia, Italy, May 2013, pp. 79–83, 15-16 May 2013.

Petra Rašić is a Ph.D. student at the Faculty of Electrical Engineering, Mechanical Engineering and Naval Architecture (FESB) at the University of Split. She completed her Master's degree in 2014, specializing in Communication and Information Technology. Her research at FESB focuses on dosimetry, specifically assessing exposure to electromagnetic fields generated by wireless power transfer systems.
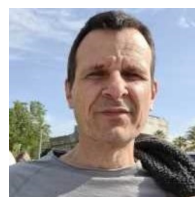
Zoran Blažević is a full professor at the University of Split, FESB, where he has been instrumental in advancing research in radio systems, channel modeling, radio propagation, antennas, and microwaves. His academic journey includes a B.S. degree obtained in 1993, followed by an M.S. in 2000 and a Ph.D. in 2005. He previously worked as a telecommunication engineer with Croatian Railways for six years.

Dragan Poljak is a full professor at the University of Split, where he earned his Ph.D. in Electrical Engineering in 1996. His research focuses on computational electromagnetics, including electromagnetic compatibility and bioelectromagnetics. With over 160 journal and 250 conference papers, he has authored several books, including two published by Wiley. A Senior IEEE member, he has received multiple awards, including the National Prize for Science (2004) and the IEEE EMC Society Technical Achievement Award (2019). He is actively involved in ITER physics and IEEE working groups.

Maja Škiljo earned her M.Sc. and Ph.D. degrees in electrical engineering from the Faculty of Electrical Engineering, Mechanical Engineering and Naval Architecture (FESB) at the University of Split in 2006 and 2014, respectively. Currently, she works as an associate professor in the Department of Electronics and Computing at the same university. Her research focuses on areas such as radio propagation, antenna design, wireless system measurements, RFID technology, and near-field wireless power transfer systems.